

# Encapsulated Nickel Nanowires Inside Plasma-treated Single-Walled Carbon Nanotubes for Urea Oxidation

Aliya R. Vildanova, Anastasia E. Goldt, Sergei V. Porokhin, Alexander G. Kvashnin, Viktor S. Baidyshev, Ilya V. Chepkasov, Fedor S. Fedorov, Kseniya A. Litvintseva, Andrey V. Lalov, Veronika A. Dmitrieva, Marina M. Tepliakova, and Albert G. Nasibulin\*

This study demonstrates a robust approach for producing Ni and Au nanowires (NWs) encapsulated by single-walled carbon nanotubes (SWCNTs), achieving lengths up to 1.2 μm. The process involves nitrogen plasma treatment to create defects in the SWCNTs, followed by the nanotubes filling with the metal precursor and its subsequent reduction. Simulations of carbon nanotube irradiation are performed to investigate the relationship between nitrogen kinetic energy and defect formation under the irradiation, revealing conditions that promote efficient nickel encapsulation. Structural analysis confirmed defect sizes ranging from 3.6 to 9.2 Å, suitable for metal precursor entry. Ni NWs exhibited excellent electrocatalytic activity in urea oxidation reactions (UOR), achieving a specific activity of 1150 A g<sup>-1</sup> at 1.7 V vs. reversible hydrogen electrode (RHE) in 2 M urea and stable performance over 1000 cycles. Comparative simulations of urea adsorption energies showed that nickel-filled SWCNTs enhance adsorption ( $-0.35$  eV) when compared to pure graphene surface ( $-0.2$  eV), demonstrating a synergistic effect of nickel and carbon structures. The role of defects in enhancing urea adsorption has also been analyzed. This work highlights the potential of SWCNTs as nano-reactors for producing high-performance catalytic materials. The findings emphasize the importance of controlled defect engineering and thermal treatment in optimizing nanowire synthesis for advanced catalytic and functional applications.

## 1. Introduction

A global search for new and alternative energy sources and the improvement of the efficiency of the existing ones often come together with waste management to decrease the carbon footprint. At this point, fuel cells capitalize on all the efforts, though mostly exploiting hydrogen as a fuel. Recent advances in room or moderate-temperature fuel cells are mostly a result of using liquid fuels, like alcohols<sup>[1]</sup> and hydrogen peroxide<sup>[2]</sup> or urea.<sup>[3]</sup> The latter compound, a component of sewage, undergoes an anodic process urea oxidation reaction (UOR),  $\text{CO}(\text{NH}_2)_2 + 6\text{OH}^- = \text{N}_2 + \text{CO}_2 + 5\text{H}_2\text{O} + 6\text{e}^-$ .<sup>[4]</sup> The thermodynamic equilibrium potential of the UOR is 0.37 V vs. a reversible hydrogen electrode (RHE), which is much lower than the 1.23 V vs. RHE required for the oxygen evolution reaction (OER), enabling a 70% reduction in energy consumption compared to traditional hydrogen production through water splitting. The use of efficient electrocatalysts for this half-reaction in electrolysis offers several advantages: energy efficiency, the possibility of recycling urea from wastewater,

and simultaneous production of high-purity hydrogen, which also opens up possibilities for creating direct urea fuel cells.<sup>[5]</sup>

The high efficiency of electrolyzers is related to the proper choice and tuning of a catalyst. While noble metals such as platinum (Pt), iridium (Ir), palladium (Pd), and rhodium (Rh) have demonstrated outstanding electrocatalytic performance in the electro-oxidation of alcohol and hydrogen peroxide, their activity toward UOR was notably low.<sup>[6,7]</sup> In comparison to noble metals, the cost-effective nickel-based catalysts exhibit higher current densities and lower oxidation potentials during the UOR,<sup>[8]</sup> exploring materials such as nickel-carbon sponges,<sup>[9]</sup> nanoribbons,<sup>[10]</sup> nanowires,<sup>[11]</sup> and nanoparticles,<sup>[12,13]</sup> supported by good stability at high potentials that are close to OER. Still, in most employed alkaline electrolytes, nickel undergoes oxidation, which might greatly deteriorate the catalyst performance,<sup>[14,15]</sup> to be also related to the agglomeration of catalyst nanoparticles, structural changes in the material, and corrosion.<sup>[16]</sup>

---

A. R. Vildanova, A. E. Goldt, F. S. Fedorov, K. A. Litvintseva,  
V. A. Dmitrieva, A. G. Nasibulin  
Laboratory of Nanomaterials  
Skolkovo Institute of Science and Technology  
Nobel Str., 3, Moscow 121205, Russian Federation  
E-mail: [A.Nasibulin@skol.tech](mailto:A.Nasibulin@skol.tech)  
S. V. Porokhin, M. M. Tepliakova  
Center for Energy Science and Technology  
Skolkovo Institute of Science and Technology  
Bolshoy Boulevard, 30, bld, Moscow 121205, Russian Federation  
A. G. Kvashnin, V. S. Baidyshev, I. V. Chepkasov  
Project Center for Energy Transition and ESG  
Skolkovo Institute of Science and Technology  
Bolshoy Boulevard, 30, bld, Moscow 121205, Russian Federation  
A. V. Lalov  
N. D. Zelinsky Institute of Organic Chemistry  
Leninsky Prospekt, 47, Moscow 119991, Russian Federation

 The ORCID identification number(s) for the author(s) of this article can be found under <https://doi.org/10.1002/smll.202507040>

DOI: 10.1002/smll.202507040

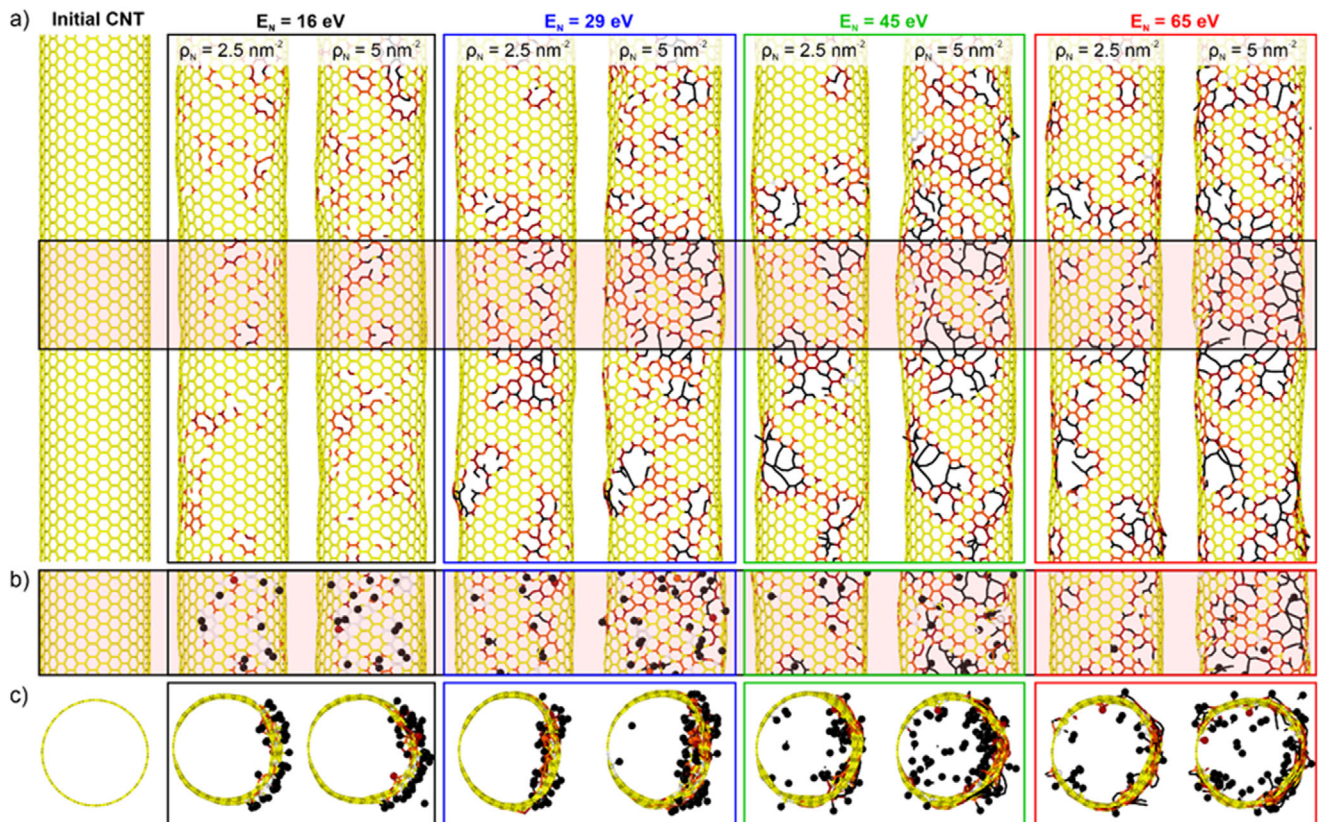


**Figure 1.** a) Structure of SWCNTs at the initial state and after the irradiation by nitrogen atoms with different energies. Snapshots at the  $2.5$  and  $5 \text{ nm}^{-2}$  density of nitrogen atoms irradiated to the surface of SWCNTs are shown depending on the energy of N. b) Selected regions with explicitly indicated nitrogen atoms as black spheres showing the distribution of nitrogen on the surface after irradiation. c) Side view of SWCNTs at the initial state and after irradiation, showing a different distribution of nitrogen inside and outside the SWCNT.

Novel approaches to the design of catalysts often presume encapsulation of active material, e.g., in carbon nanotubes,<sup>[17]</sup> carbon shell,<sup>[18]</sup> or through carburization<sup>[19]</sup> not only to protect from a corrosive environment but also to improve performance by serving as active sites.<sup>[20]</sup> This approach provides structural integrity to cope with agglomeration while maintaining good conductivity, making it a good support for the catalyst. Encapsulation within carbon nanotubes (CNTs) effectively protects confined nanomaterials, enhancing their stability and extending their longevity, providing an efficient shield from aggressive media and oxidation.<sup>[19]</sup>

Encapsulation techniques can be classified into *in situ*, i.e., in the process of nanotubes' growth (chemical vapor deposition,<sup>[21]</sup> arc-discharge),<sup>[22]</sup> and *ex situ* methods – post-synthesis treatment of nanotubes (e.g., wet chemistry approach,<sup>[23]</sup> electrochemical methods,<sup>[24]</sup> ampoule synthesis).<sup>[25]</sup> For encapsulation, first, CNTs need to be opened. Gentle oxidation of the nanotubes using gaseous or liquid oxidizers allows for the removal of CNT caps. The opening can be achieved either in air during thermal treatment<sup>[26]</sup> or in liquid by electrochemical cycling<sup>[27]</sup> or acid treatment.<sup>[28]</sup> However, these methods typically produce short nanowires (limited to  $\approx 100 \text{ nm}$  in length) which reduces the material's catalytic efficiency.<sup>[29]</sup> To address this issue, we employed plasma treatment to obtain longer structures ( $> 100 \text{ nm}$ ) and evaluate their impact on catalytic performance.

However, our choice of SWCNTs is primarily motivated by the unique advantages they offer in the context of metal nanowire encapsulation, which is not feasible with graphene-based supports.<sup>[30]</sup> In particular, structural confinement inside the tubular cavity of SWCNTs allows the formation of ultra-long, shape-controlled Ni nanowires, which are spatially stabilized and protected from aggregation or oxidation. This level of encapsulation and spatial control is hardly achievable with planar materials such as graphene or reduced graphene oxide (rGO) due to their low structural anisotropy. Moreover, graphene-based systems often suffer from insufficient long-term stability under harsh alkaline UOR conditions. In particular, rGO can undergo structural degradation due to oxidation and delamination.<sup>[31]</sup> The interaction between Ni particles and rGO is relatively weak, which leads to the detachment or migration of active species during cycling, drastically reducing activity and durability.<sup>[32]</sup>

The confinement effect and defect sites with effective electron transfer along the SWCNTs and protection of ions from nanoparticle clumping facilitate the creation and stability of the high-valence NiOOH form under high anode potential (up to  $1.4 \text{ V}$  vs. RHE), crucial for UOR.<sup>[33,34]</sup> In addition, the close contact between nickel and the conductive carbon within the SWCNTs guarantees low-resistance pathways, resulting in improved performance.

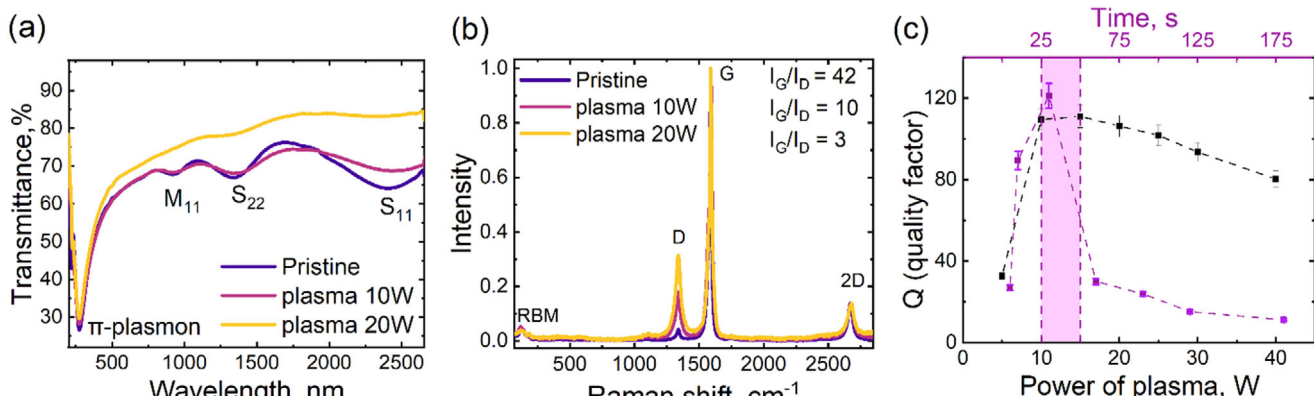


**Figure 2.** Characterization of pristine and plasma-treated SWCNT films during 30 s: a) UV-vis–NIR spectra and b) Raman spectra. c) Dependence of the quality factor on plasma duration time (at fixed power of 10 W) and plasma power (at fixed treatment time of 30 s).

Here, we propose a method combining efficient nitrogen plasma treatment of SWCNTs and subsequent growth of nickel nanowires inside the tubes. Computational modeling of nitrogen plasma irradiation provided insights into defect formation on SWCNT surfaces, revealing that energies up to 65 eV optimize defect density and facilitate metal encapsulation. The results highlight the crucial role of plasma treatment in defect formation on the SWCNT surfaces, opening, enhancing their filling capacity, increasing the adsorption of the analyte, and enabling the synthesis of long nickel NWs in comparison to thermal treatment. The catalytic performance in terms of stability and mass activity of the resulting Ni NWs encapsulated in nitrogen plasma-treated SWCNTs (Ni NWs@N-SWCNTs) was successfully demonstrated for urea oxidation in an alkaline medium. The combination of excellent electrical conductivity, chemical stability, and tailored adsorption properties of the carbon nanomaterial ensures its durability as a support for electrocatalysis. This innovative material shows significant promise for applications in urea-based fuel cells/electrolyzers since the anodic reaction is the same, thereby enabling efficient hydrogen production.

## 2. Results and Discussion

### 2.1. Experimental Part

SWCNT films with a transmittance of 65% at 550 nm (thickness about 44 nm) were synthesized by the aerosol chemical vapor deposition (CVD) method and transferred onto glass substrates using a dry transfer technique (Characterization of SWCNTs film, Text S2 and Figure S1, Supporting Information).<sup>[35]</sup> The SWCNTs film mass was measured to be  $0.5 \pm 0.2 \mu\text{g cm}^{-2}$ . Nitrogen plasma treatment was performed at power range of 5–40 W and durations of 5–150 s. Nickel and gold NWs were incorporated into the SWCNTs by dip-coating method from precursor solutions, and in the case of nickel, reduced by hydrazine hydrate, with nickel nanowire content estimated to equal 39–55% of the film mass (Text S3, Supporting Information. Nickel nanowires inside SWCNTs synthesis). The effect of nitrogen plasma treatment on the structural and electronic properties of the films was characterized using optical techniques, including Raman spectroscopy, UV-vis–NIR, FTIR, and EPR spectroscopy. Additionally, struc-

tural and compositional analysis of the samples was carried out using TEM, HRTEM, XPS, electron diffraction pattern, and EDX (details of material characterization are presented in Text S4, Supporting Information).

### 2.2. Simulation of the Irradiation of SWCNT by Nitrogen

To define the formation of different defects on the surface of SWCNTs, we have simulated the irradiation of SWCNT by nitrogen atoms with different energies (Text S7, Supporting Information. Molecular dynamics simulations). The atomic structure of the simulated SWCNTs is shown in Figure 1a, together with SWCNTs after irradiation by N atoms with different kinetic energies, 16, 29, 45, and 65 eV. For each energy, the snapshots with two densities of irradiated atoms are presented. One can see that low-energy irradiation leads to the formation of vacancies, while all the nitrogen atoms are located on the surface of the SWCNT. Nitrogen energy of 16 eV is not sufficient to punch the tube (Figure 1b,c). In this case, the formed defects are small, and nitrogen atoms on the surface will prevent nickel from entering the SWCNT through the defects. Increasing energy to 29 eV leads to the formation of extended defects rather than point defects. Additionally, areas of major structural damage are visible. The nitrogen atoms can be observed inside the tube (Figure 1c). Higher energies (45 and 65 eV) lead to serious damage to the structure of the SWCNT, forming long chains of defects without nitrogen atoms on the surface (Figure 1b). These defects may serve as a way for nickel to enter inside the tube. However, one can propose that further increasing the energy of irradiated nitrogen will lead to the formation of a larger number of defects. We have calculated the defectiveness of the SWCNT as the number of defective atoms with respect to the total number of atoms in the tube formed after irradiation, depending on the energy, as shown in Figure S3 (Supporting Information). At the energies above 65 eV, the dependence approaches saturation, and the number of defects does not increase. This is caused by the decreasing scattering cross-section with increasing speed of nitrogen atoms. Additionally, simulation of irradiation shows that low-energy nitrogen atoms create point defects on the surface, while high-energy atoms form extended defects, with defect sizes ranging from 3.6

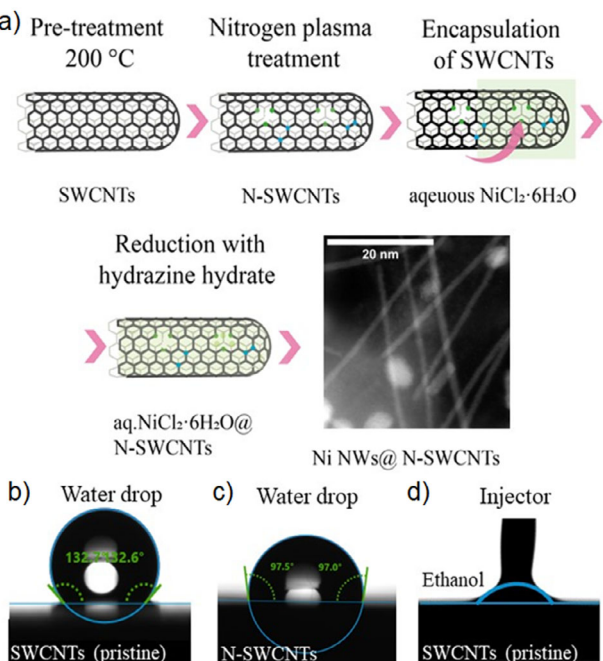


**Figure 3.** A schematic illustration of the preparation of SWCNTs filled with Ni NWs a). Contact angle measurements between, 5  $\mu\text{L}$  droplet: b) water droplet and pristine SWCNTs, c) water droplet and SWCNTs treated in nitrogen plasma (during 30 s at 10 W), d) ethanol droplet and pristine SWCNTs.

to 9.2 Å, significantly larger than the nickel atom radius (1.24 Å) (Refer to Text S 7–9. Simulation of irradiation of SWCNT by nitrogen). Thus, the most defective SWCNT can be obtained with energy up to 65 eV.

Studying the opening of the carbon nanotubes was carried out to optimize two key goals: to minimize the defect level to keep high electrical conductivity and to maximize filling capacity. In our experiments, we implemented nitrogen plasma treatment with subsequent dip-coating of the films into the nickel solution. It was found that increasing the plasma power and processing time naturally led to the growth of defects in the SWCNTs (Figures S3 and S4, Supporting Information), while higher plasma powers result in wall collapse or damage that inhibits filling.

The defects introduced in SWCNTs by nitrogen plasma treatment were characterized using a combination of spectroscopic techniques. UV-vis-NIR spectroscopy showed suppression of Van Hove singularities and an overall increase of transmittance, reflecting SWCNT etching and electronic structure disturbance due to the presence nitrogen defects (Figure 2a; Figure S5b, Supporting Information). This finding was further supported by EPR spectrum analysis, which revealed characteristic g-values. The EPR spectrum of the initial SWCNTs (Figure S7a, Supporting Information) shows a signal at  $g \approx 2.06$ , characteristic of unpaired electrons in lattice defects, without noticeable impurities. After the treatment with nitrogen plasma (Figure S7b, Supporting Information), the signal is noticeably broadened due to enhanced spin-spin interactions and relaxation, and novel spectral components appear at  $g \approx 2.21$  (nitrogen-containing paramagnetic cen-

ters) and a weak feature at  $g \approx 1.88$  (traces of iron from the catalyst). Collectively, the spectrum reflects a complicated defective structure induced by plasma modification.<sup>[36]</sup> Importantly, these data corroborate XPS analysis results (Figure S8, Supporting Information) related to the defects formation upon the plasma treatment. The analysis confirms the presence of nitrogen-containing defects formed during plasma treatment, as reported in.<sup>[37,38]</sup> According to the literature data, peaks at 285.7, 288.1, and 289.4 eV can be assigned to carbon forming C—OH/C—N, C=O, and O=C=O bonds, respectively.<sup>[39,40]</sup> The treatment in plasma indeed leads to the formation of defects in the structure of SWCNTs: a peak at 399.6 eV could be assigned to nitrogen in amino group, pyridinic group, and a peak at 400.6 eV to nitrogen in pyrrolic group.<sup>[37]</sup> FTIR analysis (Figure S9, Supporting Information) confirms nitrogen incorporation into the SWCNT structure after the plasma treatment through the appearance of N—H and C—N stretching peaks and N—H bending vibrations, along with the  $\text{sp}^3$  C—H bands indicating defect formation and disruption of the  $\pi$ -system.<sup>[41]</sup>

To quantitatively assess the optoelectronic properties of the various SWCNT films, we have compared their equivalent sheet resistances, denoted as  $R_{90}$ , which is calculated for a film with a transmittance of 90% at a wavelength of 550 nm:

$$R_{90} = R_s * \frac{A_{550}}{-\log_{10}(0.9)} \quad (1)$$

where  $A_{550}$  and  $R_s$  are the absorbance (at 550 nm) and the sheet resistance of the films.<sup>[35]</sup>

While pristine SWCNTs typically have an equivalent sheet resistance of  $\approx 644 \pm 32 \Omega \text{ sq}^{-1}$ , after plasma treatment at 10 W and 30 s, SWCNT films exhibit  $R_{90}$  values approaching  $1600 \pm 12 \Omega \text{ sq}^{-1}$  (Figure S10b, Supporting Information). This can lead to the formation of defects in the crystal lattice of SWCNTs, such as vacancies, displacements of carbon atoms, and the incorporation of nitrogen into the interatomic spaces (Text S10, Supporting Information).<sup>[36,42]</sup> These defects disrupt the continuity of conductive pathways in the nanotube structure. Additionally, the quality of the SWCNTs was evaluated by Raman spectroscopy. The Raman spectrum of the untreated SWCNT films (Figure 2b) generally features the chirality-sensitive radial breathing mode (RBM)  $\approx 100$ –500 cm<sup>−1</sup>, a D-mode peak near 1340 cm<sup>−1</sup>, a graphitic G-mode peak near 1590 cm<sup>−1</sup>, and a 2D-mode peak at 2680 cm<sup>−1</sup>. In comparison with pristine SWCNTs, the plasma-treated film at 10 W for 30 s demonstrated a decrease in the  $I_G/I_D$  ratio by a factor of 4, indicating an increase in the tube defectiveness. To find the optimal conditions for the SWCNT treatment by plasma, we introduce the quality factor, which is the product of the defectiveness and conductivity of carbon nanotube films:

$$Q = \frac{R_{90}}{R_{90 \text{ pristine}}} * \frac{I_G}{I_D} \quad (2)$$

Plasma treatment within the power range of 10–15 W and a duration of 25–50 s effectively induces defect formation in SWCNTs while minimizing structural degradation and preserving moderate sheet resistance (Figure 2c). Computational modeling of nitrogen plasma irradiation and defect formation analysis

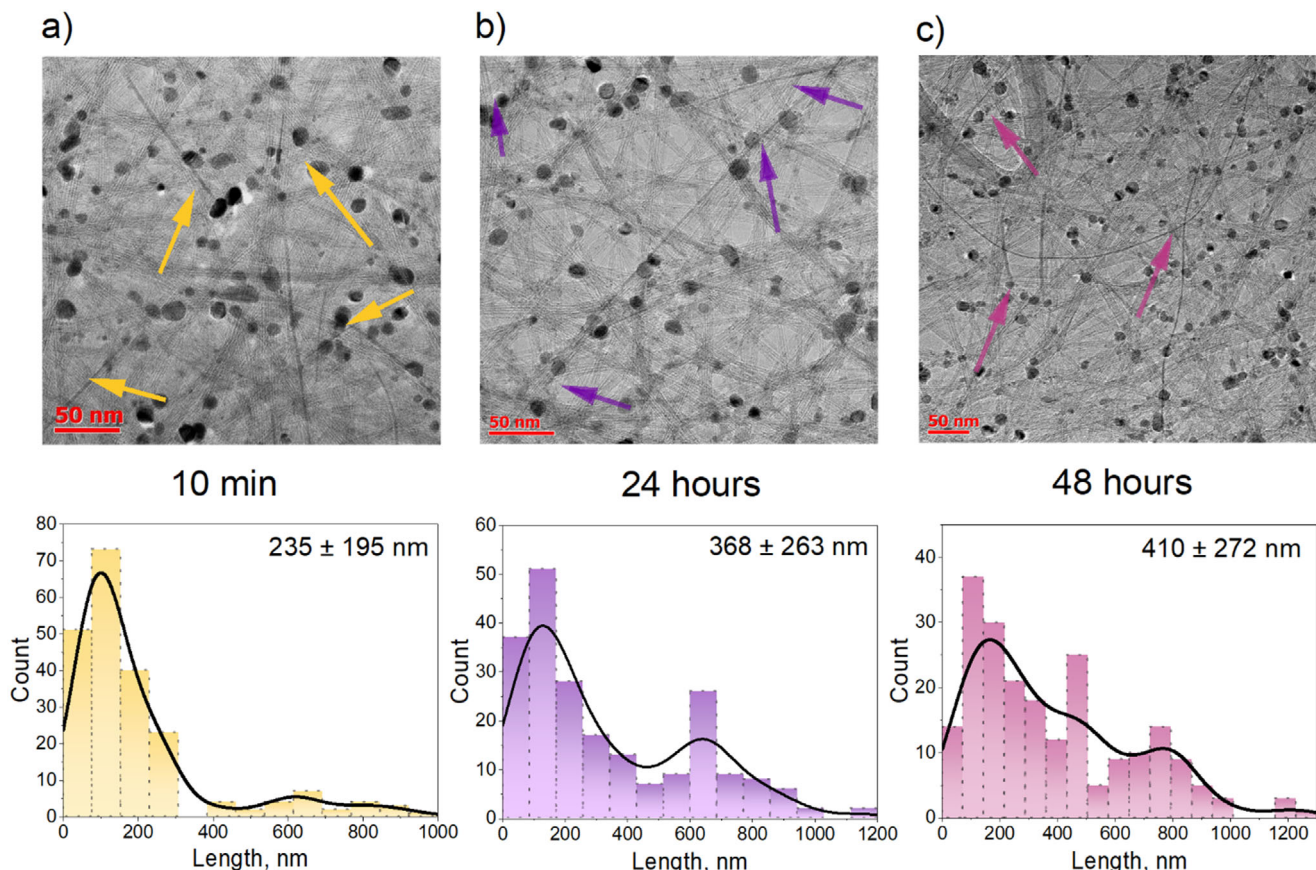


**Figure 4.** TEM images of SWCNTs treated with plasma (during 30 s at 10 W) filled with 30 mM  $\text{NiCl}_2$  in water and reduced with hydrazine during different immersion times: a) 10 min, b) 24 h, c) 48 h, and length distributions of nanowires. The arrows indicate nickel nanowires inside SWCNTs.

identified the optimal defect configuration (45–65 eV), facilitating maximal filling of the nanotubes. These parameters were specifically chosen to ensure the efficient opening of SWCNTs for subsequent filling applications.

### 2.3. Filling SWCNTs with Nickel

To assess the impact of defects on SWCNT filling, we employed gold as a model object and utilized plasma treatment under selected parameters. Subsequent dip-coating into a gold salt solution induced *p*-doping, evidenced by blue shifts in Raman G-mode peaks (about  $20\text{ cm}^{-1}$ ) and the disappearance of  $S_{11}$ ,  $S_{22}$ , and  $M_{11}$  peaks in UV-vis-NIR spectra (Figure S13, Supporting Information). Gold nanowires with lengths up to 90 nm formed within 10 min, with no significant length increase upon extended immersion (Text S13, Supporting information). Following this, we proceeded to explore the process of filling nanotubes with nickel.

The protocol of nanowire growth inside SWCNTs after opening first includes the immersion of carbon nanotubes into a nickel solution. Subsequently, after the reduction of nickel within SWCNTs with hydrazine, nucleation occurs and facilitates the following growth of nanowires inside SWCNTs (Figure 3a). The reaction between SWCNTs and  $\text{Ni}^{2+}$  is not thermo-

dynamically favorable due to the lack of electromotive force to drive it, unlike the interaction between SWCNTs and  $\text{Au}^{3+}$  (Table S5, Supporting Information).<sup>[43]</sup> Therefore, we have utilized hydrazine hydrate as a reducing agent, which is both affordable and easier to use compared to alternatives such as sodium borohydride or reduction in a hydrogen flow at elevated temperatures.<sup>[44]</sup>

In this study, solvents containing gold or nickel ions are introduced by a capillary driving force. Two parameters affect filling: contact angle ( $\theta$ ) should be less than  $90^\circ$  (capillary uptake even if  $\theta > 90^\circ$ , as long as  $1\text{ R}^{-1} > -\cos \theta$ , where  $R$  is pore radius), and the surface tension, which should be less than  $100\text{ mN m}^{-1}$  to fill carbon nanotubes through the capillary effect.<sup>[45]</sup> To investigate the impact of plasma treatment on surface properties, the contact angle of water was measured for pristine (Figure 3a) and plasma-treated SWCNTs (Figure 3c; Table S2, Supporting Information). Plasma treatment significantly reduced the contact angle from  $132^\circ$  to  $97^\circ$ , indicating enhanced surface hydrophilicity. In contrast, when absolute ethanol was applied (Figure 3d), complete wetting occurred, confirming the high surface energy and strong solvent affinity of SWCNTs after the treatment. Based on these data, the maximum filling length is calculated (Table S3, Supporting Information) to assess which of the solvents has a greater filling capacity (Text S11, Supporting Information. Selection of solvent).

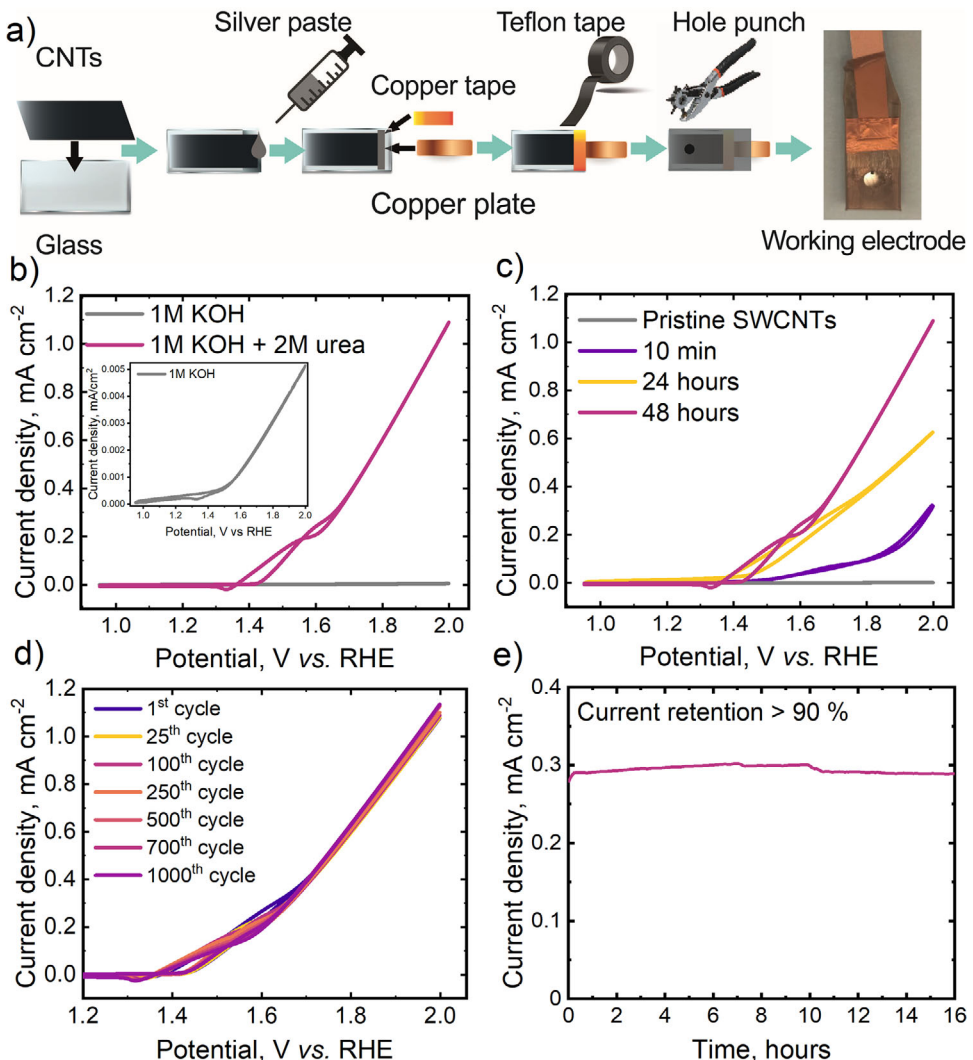


**Figure 5.** Cyclic voltammograms (CV) for the produced Ni-nanowires inside carbon nanotubes,  $50 \text{ mV s}^{-1}$  scan rate, and  $25^\circ\text{C}$ : a) working electrode preparation scheme, b) CVs in the absence and presence of urea, 2 M for sample with 48 h immersion time at 100<sup>th</sup> cycle; c) CV acquired for the samples produced using different immersion times, d) CV recorded during 1000 cycles and e) chronoamperometry test at 1.65 V vs. RHE for the sample produced using 48 h immersion time.

The distribution of the nickel nanowires, depending on the solvent studied based on TEM images (Figure S11, Supporting Information). Despite the water's contact angle indicating poor wetting, the use of an aqueous precursor solution results in longer nanowires up to  $1.2 \mu\text{m}$ . Experimental results show that after plasma treatment, the higher surface hydrophilicity of SWCNTs improved their interaction with filler solution. Recent research highlights that the filling rate of SWCNTs by water significantly increases with extended immersion time. We analyze the dependency between the time of dipping SWCNTs into the filler solution (Figure 4) and the length of the nanowires using the Kernel Density Estimation (KDE). At first, we observe a slight increase in the length of the nanowires, almost reaching a plateau in the cases of 24 h (Figure 4b) and 48 h (Figure 4c). When comparing the density of long nanowires, filling during longer immersion time yields similar results, with mean KDE-based lengths of  $368 \pm 263$  and  $410 \pm 272 \text{ nm}$ , respectively.

The high-resolution TEM (HRTEM) image S14a reveals dark regions inside the carbon nanotube that correspond to NWS. From this image, it is possible to calculate the interplanar distance of such a structure and examine the electron diffraction pattern, which displays clear diffraction rings, indicating the crystallinity of the encapsulated phase (Text S14, Supporting Information). The dark field mode (HAADF-STEM) image S14b confirms the distribution of nickel NWs along the carbon nanotubes. The obtained  $d$ -spacing from both methods ( $\approx 0.203 \text{ nm}$  and  $\approx 0.177 \text{ nm}$ ) corresponds well to the (111) plane of face-centered cubic (FCC) Ni, in agreement with literature values  $0.2034 \text{ nm}$  for the (111) plane and  $0.176 \text{ nm}$  for the (200) plane. The electron diffraction pattern further supports the crystalline nature of the encapsulated phase. The energy dispersive spectrum (EDS) inset (Figure S14b, Supporting Information) and the elemental composition table (Table S4, Supporting Information) show a high carbon content (89.9%), which is due to the presence

**Table 1.** Comparative characteristics of existing nickel-based catalysts for urea oxidation.

Catalyst material	Current density [mA cm <sup>-2</sup> ]	Potential [V vs.RHE]	Electrolyte and concentration of urea	Mass loading [µg cm <sup>-2</sup> ]	Mass activity [A g <sup>-1</sup> ]	Refs.
Amorphous Nickel Oxide Encapsulated on N-doped carbon Nanosheets	10	1.38	1 M KOH 0.33 M urea	1500	15.5	[52]
Nickel nanoparticles embedded in carbon nanotubes	45.8	1.5	1 M KOH 0.5 M urea	2850	53.6	[33]
Ni-incorporated carbon nanofibers	30	1.6	1 M KOH 2 M urea	1014	74	[53]
Nickel-Doped Carbon Dots	100	1.38	1 M KOH 0.33 M urea	2000	900	[54]
Nickel nanoparticles-decorated graphene	150	1.78	1 M KOH 2 M urea	1071	298	[12]
NiFe <sub>2</sub> O <sub>4</sub> supported on graphene oxide	26.6	1.5 V for 10 mA cm <sup>-2</sup>	1 M KOH + 1 M urea	285	10	[55]
Nickel particles encapsulated in carbon shells	100	1.55	1 M KOH + 0.5 M urea	7142	333	[18]
Ni/NiS@CP (on the carbon paper)	50	1.55	0.1 M KOH + 0.33 M urea	750	115	[56]
CoP@P, NCNTs on Ni foam	200	1.57	0.1 M KOH + 0.33 M urea	8750	23	[57]
Nickel nanowires inside plasma-treated single-walled carbon nanotubes	0.39	1.7	1 M KOH 2 M urea	1.15	1150	Current work

of carbon nanotubes. Nickel (1.47%) and iron (0.42%) are also detected.

Although the formation of nickel nanowires was confirmed by TEM, electron diffraction pattern, and EDX, the composition and structure could not be verified directly by XPS or XRD due to the inherently low mass loading of the active material and the nature of the thin-film samples.<sup>[46]</sup> Specifically, no distinct Ni 2p peaks were observed in the XPS spectra. Figure S8e (Supporting Information) shows the Ni 2p<sub>3/2</sub> spectra of the studied samples. In the Ni 2p<sub>3/2</sub> spectra of samples, unwashed Ni-NWs@N-SWCNTs showed an intense peak attributed to the excess amount of the catalyst on the surface, but after washing, the intensity was decreased. A peak was observed at a binding energy of 855.9 eV before and after the electrochemical test, which could be assigned to nickel in Ni(OH)<sub>2</sub>/NiOOH.<sup>[47–49]</sup> Also, at 861.7 eV a broad satellite peak was observed. Additionally, the XRD signal showed no clear signal, which is associated with an amorphous carbon structure after the plasma treatment. These limitations are discussed in detail in the S.I. (Text S14, Supporting Information).

To identify the nature of the nanoparticles observed in the samples and to exclude their influence on future electrocatalytic measurements, we analyzed HRTEM (Figure S16a, Supporting Information). The results confirmed the presence of  $\alpha$ -Fe nanoparticles encapsulated in a thin Fe<sub>3</sub>C shell, consistent with residues from CVD growth.<sup>[50]</sup> EDX map with EDX spectrum (Figure S16b, Supporting Information) confirmed the presence of iron NPs over the samples.

Additionally, we examined the effect of surface hydrophilicity under various treatment parameters, the influence of concentration, and solvent-wetting parameters. Moreover, the influence of filling rate and solution temperature on nanowire formation was investigated. Details on the methodology and results are provided in the Supporting Information (see Text S10–S15, Supporting Information).

## 2.4. Electrochemical Study

SWCNT films with encapsulated Ni NWs were dry-transferred onto glass slides ( $1 \times 1 \text{ cm}^2$ ), densified with ethanol, and connected to a copper plate using silver paste and copper tape; the assembly was coated with Teflon tape (Figure 5a). Electrochemical measurements were carried out in 1 M KOH with varying urea concentrations (0.5–2 M) using a three-electrode cell (Ag/AgCl reference, Pt counter) at 25 °C under N<sub>2</sub> flow.

Figure 5b illustrates the cyclic voltammogram behavior of the Ni-nanowires encapsulated in carbon nanotubes in the presence of urea. The addition of 2 M urea significantly increases the anodic current density to 0.39 mA cm<sup>-2</sup> at a potential of 1.7 V vs. RHE. This represents a 80-fold increase compared to the pristine nanotubes, indicating the electrocatalytic activity of Ni NWs@N-SWCNTs electrode toward urea oxidation.

As the aforementioned results in this work show, increasing the film's immersion time in the solution leads to an elongation of the nanowires. It has been demonstrated that there is a tendency for the current density of nanowires to increase as their length is elongated (Figure 5c). Ni NWs@N-SWCNTs with 48 h immersion time show a 4-fold increase in current density when compared to Ni NWs@N-SWCNTs with 10 min immersion time, synthesized through the same procedure. Subsequent analysis reveals that using a urea concentration of 2 M yields the most valuable performance (see details in Text S17, Supporting Information). Furthermore, reproducibility tests have confirmed that nanowires are formed consistently and reliably across multiple trials (Figure S24a, Supporting Information).

Additionally, Ni NWs@N-SWCNTs catalyst shows excellent stability after the initial activation stage: over 98% of current density is retained after 1000 cycles, with minimal changes observed beyond the 250th cycle. The sharp changes in current between the 1st and 100th cycle result from the electrochemical removal of residual Fe nanoparticles. As reported,<sup>[24]</sup> iron is gradually leached out during the first 10–15 cycles under anodic

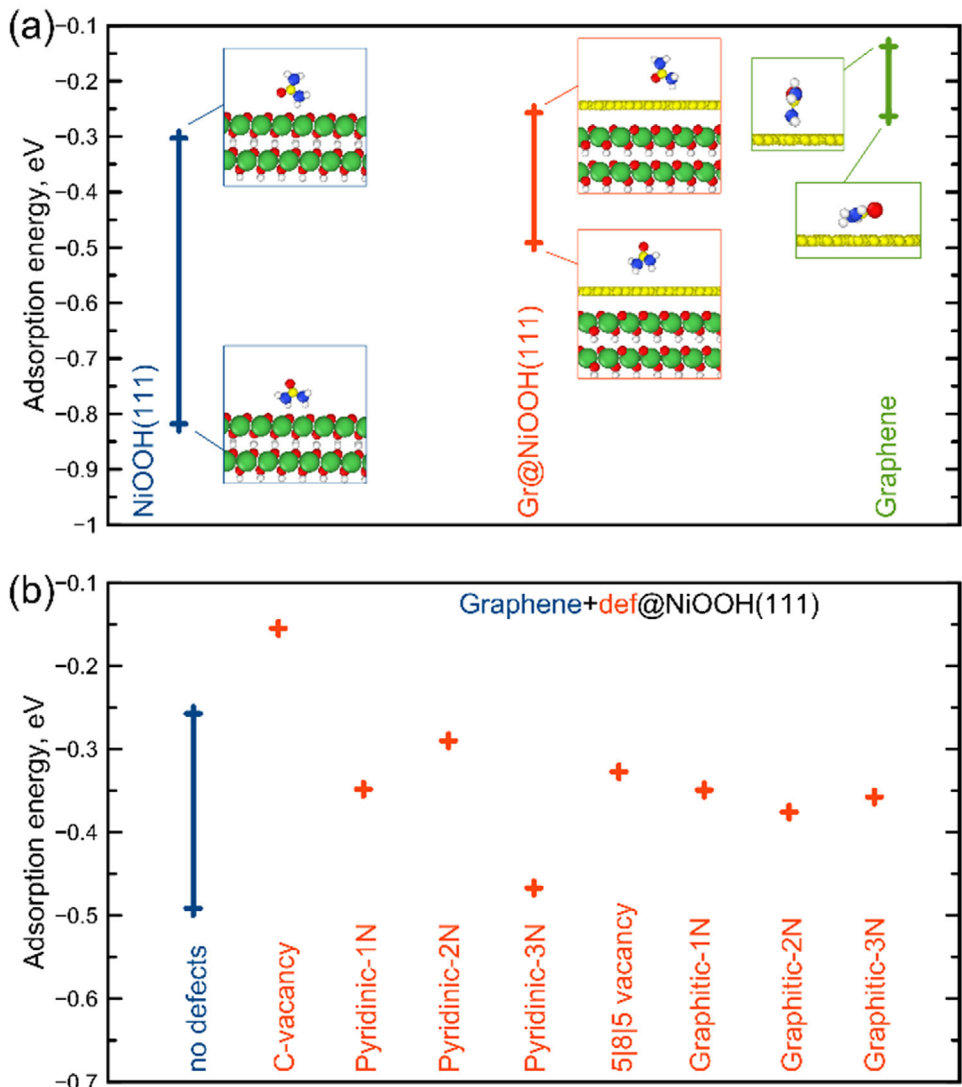


**Figure 6.** a) Adsorption energy of urea on NiOOH(111), graphene-on-NiOOH(111), and graphene substrates. The insets show the atomic arrangement of urea on top of these surfaces. b) Adsorption energy of urea on the graphene-on-NiOOH(111) with different types of defects. Red crosses show the adsorption energy of the urea with the lowest energy.

polarization. Beyond this, the system reaches a stable electrochemical state, as confirmed by first-derivative analysis (Figure S20 and stability test Figure S21, Supporting Information), indicating the absence of further degradation. To access the effect of the iron influence on the catalytic nature and exclude the synergistic effect, the concentration of iron ions in the electrolyte after stability test was measured. The absorption signal in the post-stability electrolyte (Figure S27, Supporting Information) corresponds to an estimated concentration of  $\text{Fe}^{3+} \approx 2.5 \times 10^{-3} \mu\text{M}$  ( $\approx 2.5 \times 10^{-9} \text{ M}$ ), which is equal to  $\approx 1.4 \times 10^{-10} \text{ g ml}^{-1}$  for iron.

Indeed, at first glance, the strategy of nickel confinement inside SWCNT may seem to contradict the task of maximizing the active surface area. However, the key goal of our work is to demonstrate an approach for encapsulation that, as a result, enables to maintain its catalytic activity for a long time. However, this is not a disadvantage, but rather a fundamental and deliberate compromise inherent in the concept of structural con-

finement. In traditional Ni catalysts with high metal loading, significant initial activity is achieved, but such systems rapidly degrade due to aggregation, oxidation, and leaching. In the proposed architecture, high stability and durability are supported by the preservation of more than 98% of the activity after 1000 cycles (Figure 5d). In Figure 5e, the chronoamperometry test demonstrates high stability of the catalyst over 16 h of continuous operation under optimized conditions with a Teflon-coated electrode and more than 90% current retention and minor fluctuations attributed to electrolyte depletion and formation of bubbles on the surface. In contrast, without the Teflon coating, the current retention after 1.5 h is reduced to  $\sim 80\%$ , indicating the importance of the electrode preparation role (Figure S23, Supporting Information). The use of the Teflon coating, as described in Text S18 (Supporting Information), prevents film delamination during stability tests. All these results demonstrate that the confinement strategy works as a catalyst protection method,

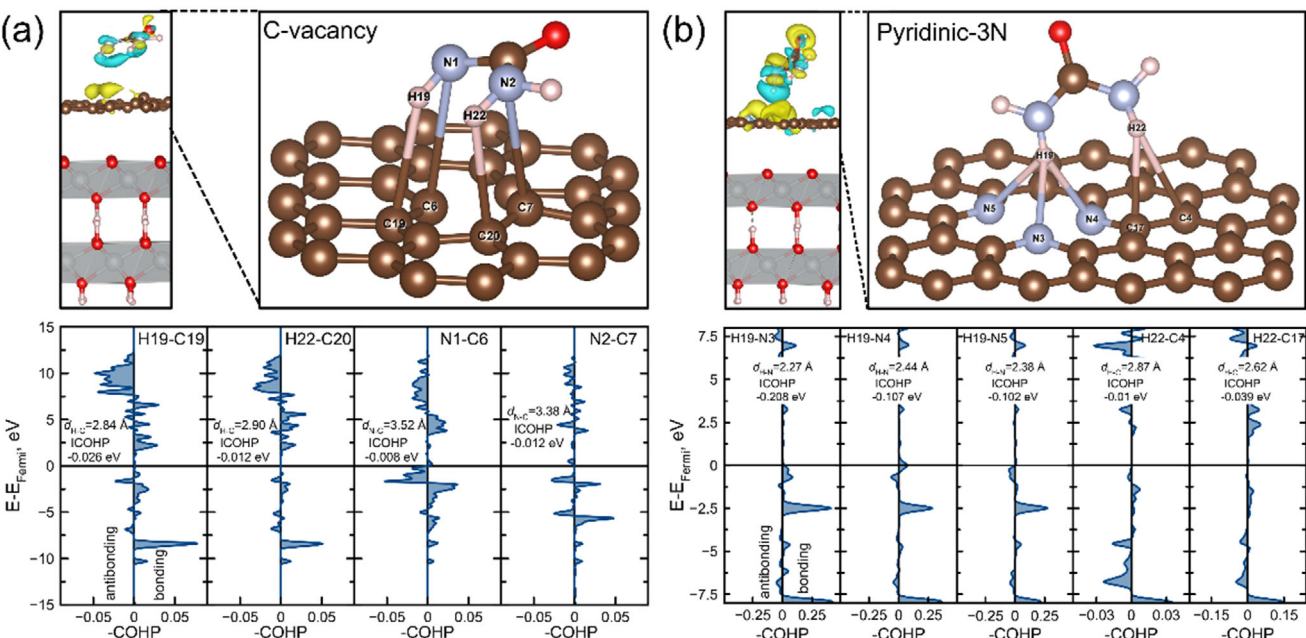


**Figure 7.** Analysis of charge redistribution and chemical bonding (-COHP) between the urea molecule on top of the (a) graphene with a vacancy defect, and (b) graphene with pyridinic-3N defect. The isosurface level for charge is  $0.005 \text{ e}/\text{\AA}^3$ . The number of atoms between which COHP is calculated, along with the Integrated COHP values, are shown in the figures.

ensuring long-term operation, which is critical for practical application. The retained Raman shift ( $\sim 8 \text{ cm}^{-1}$ ) after 1000 CV cycles indicates the preservation of the encapsulated metallic phase. Figure S25e,f (Supporting Information), shows Raman features near  $480$  and  $560 \text{ cm}^{-1}$ , which are reported in the literature as characteristic of NiOOH formation under UOR conditions<sup>[51]</sup> are commonly used as indirect evidence of NiOOH formation. We propose similar surface transformations occurring under alkaline conditions with Ni NWs@N-SWCNT catalyst. Furthermore, TEM images (Figure S25h,i, Supporting Information) show that nanowires remain structurally confined within the SWCNTs, despite partial overlayer formation that confirms the structural integrity of such nano-confined catalyst. In addition, the XPS results indicate that before the stability test (after catalyst stabilization during the first 20 cycles and iron removal), a peak which shows the preservation of the catalyst structure at a binding energy of  $855.9 \text{ eV}$  before and after the electrochemical test is maintaining.

Finally, Ni NWs@N-SWCNTs electrode material exhibits relatively high mass activity  $1150 \text{ A g}^{-1}$  at an oxidation potential of  $1.7 \text{ V}$  vs. RHE, which is higher than graphene decorated with nickel nanoparticles, with  $298 \text{ A g}^{-1}$  at  $1.78 \text{ V}$  vs. RHE and other nickel-based nanostructures (Table 1).

While the measured geometric current density is determined by the SWCNT film thickness, the latter might be modulated to help enhance the current. At the same time, SWCNT films alone do not show a notable activity towards UOR, raising a question of the density of encapsulated Ni nanowires. Thus, at a given distribution of encapsulated nanowires, we consider mass loading of Ni as a major parameter to describe the activity (in comparison to the negligible mass of SWCNTs) while the film of SWCNTs plays the role of conductive matrix. In our work, we used

SWCNT films with an average thickness of about  $44 \text{ nm}$  after the synthesis. Such a film is represented by an aerogel structure before the chemical treatment and immersion in the electrolyte. So, the film thickness determines the geometric current density and helps to tune the balance between active phase loading, conductivity, and mass transfer. Thicker layers increase the number of active centers per geometrical area but can limit transport and reduce efficiency, while thinner layers provide better electrolyte accessibility but reduce the overall loading and conductivity (while the density of Ni-encapsulated wires should remain similar).<sup>[58,59]</sup>

## 2.5. Analysis of Adsorption Characteristics

We propose that this structural environment, Ni confined within defect-functionalized SWCNTs, provides a favorable platform for the formation of active NiOOH species and supports the proposed mechanism described in prior studies in detail.<sup>[11,33,60]</sup> To calculate the adsorption energy of urea molecules on SWCNTs filled with Ni atoms, we have simulated three types of flat slabs, namely graphene, NiOOH(111), and graphene-on-NiOOH (111). The latter one (graphene-on-NiOOH(111)) simulates the filled SWCNT. For each surface, four different configurations of the urea molecule are considered, as the adsorption energy strongly depends on the position of the molecule on the surface. The calculated ranges of adsorption energies are shown in Figure 6a. Adsorption of urea on graphene has an average adsorption energy of  $-0.2 \text{ eV}$ , while the addition of NiOOH under the carbon layer decreases the adsorption energy to an average value of  $-0.4 \text{ eV}$ . For comparison, the pure NiOOH(111) surface is also considered to have an even lower adsorption energy of  $\approx -0.66 \text{ eV}$ . Such a

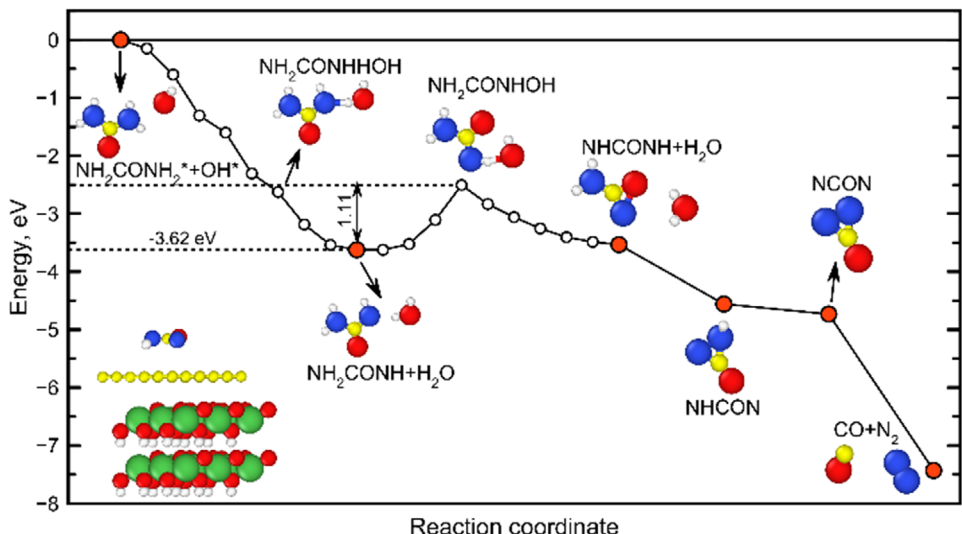


**Figure 8.** Energy profile of the reaction cascade of urea oxidation on the Gr@NiOOH(111) surface. Red points show steps corresponding to hydrogen detachment from urea by OH. White points denote configurations obtained by the NEB method. Only configurations of the molecule on the surface are shown, while the Gr@NiOOH(111) substrate is hidden.

high adsorption energy is typical of metallic sites, as in the case of WN.<sup>[61]</sup>

During the irradiation of SWCNT with nitrogen, different types of defects were observed, as shown in Figure S4 (Supporting Information). The appearance of these defects will influence adsorption properties, which differ from ideal cases considered previously. We calculated adsorption energy of urea on graphene, graphene-on-NiOOH(111) substrates, depending on the type of defect. Here, the following defects are considered: carbon monovacancies, linear 5|8|5 defects and graphitic and pyridinic defects at different concentrations. The calculated dependencies of adsorption energies of urea on graphene with different types of defects are shown in Figures S28–S30 (Supporting Information).

It can be seen that the presence of any type of defect in graphene leads to a reduction in the adsorption energy of urea (binding becomes stronger). After irradiation, defects are necessarily present in the structure, and they affect the adsorption properties. Therefore, calculations of the adsorption energies of urea are necessary. We calculated the dependence of the adsorption energy of urea on the graphene-on-NiOOH(111) substrate with nitrogen and vacancy defects in graphene, as shown in Figure 6b. As can be seen, the presence of these defects does not significantly affect adsorption energy compared to pure graphene-on-NiOOH(111) substrate. However, these values are still approximately half as low as pure graphene within a nickel-based substrate ( $-0.2$  eV vs.  $-0.35$  eV). The strongest binding (lowest adsorption energy) is for graphene with two nitrogen atoms in neighboring positions (pyridinic-3N in Figure 6b). The highest energy belongs to graphene with a monovacancy.

To deeply understand the origin of significant differences between the adsorption energies for graphene with different types of defects, we perform the Crystal Orbital Hamilton Population (COHP) analysis. This allows us to analyze the chemical bonding between the adsorbed molecule and the surface. We carefully analyze two cases of weak adsorption (Graphene+C-vacancy@NiOOH(111)) and strong adsorp-

tion (Graphene+Pyridinic-3N@NiOOH(111)), according to the data from Figure 6b. Detailed information about charge redistribution for other types of defect is presented in the Supporting Information.

Here in Figure 7 the computed charge redistribution and COHP dependencies are shown for C-vacancy and pyridinic-3N defects in graphene with adsorbed urea. One can see that the presence of pyridinic-3N defect leads to significant charge redistribution compared to the C-vacancy. The larger the charge flows to the graphene, the stronger the chemical bond is. Strength of chemical bonds is analyzed by computing ICOHP depending on the energy. This data is used to calculate the integrated COHP value of each bond, which can be associated with bond strength. Here, one can see that for C-vacancy, the values of ICOHP are  $-0.008$  and  $-0.012$  eV between carbon atoms of graphene and nitrogen atoms of urea. Small negative values denote weak chemical bonding, which directly relates to the low adsorption energy. In contrast to C-vacancy, the pyridinic-3N defect possesses much higher ICOHP values (one order of magnitude higher), see Figure 7b. In this case, the major contribution to the bonding comes from N-H bonds with ICOHP from  $-0.208$  to  $-0.102$  eV. Obtained information about the chemical bonding of urea with graphene lying on top of NiOOH(111) surface with two types of defects allows us to explain the role of defects obtained during the irradiation in the stronger adsorption of urea. Such large-area defects with nitrogen edges are the most common after the nitrogen irradiation, as was shown by our simulations. Big number of nitrogen-based defects together with strong adsorption of urea explain the effect observed in the experiment.

To deeply understand the adsorption characteristics of the considered systems and the synergetic effect of graphene and NiOOH (111), we calculate the energy barrier of several steps of the urea oxidation reaction. According to the ref.,<sup>[62]</sup> we consider the direct electrooxidation mechanism of urea. The key role here is played by the OH group, which detaches hydrogen from the urea molecule.

We simulate the presence of the OH group on the surfaces of graphene, NiOOH(111), and Gr@NiOOH(111) together with urea. Nudged elastic band calculations are used to calculate the energy barrier for the first and second steps in the reaction cascade. In total, the energy barriers for the subsequent detachment of two hydrogen atoms are calculated. The resulting energy diagram is shown in **Figure 8**. One can see that detachment of the first H from urea occurs without any energy barrier. Detaching hydrogen from a urea molecule placed on the surface of Gr@NiOOH(111) is more energetically favorable. Energy difference is 3.62 eV. The second step of hydrogen detachment occurs with a relatively low activation barrier of 1.11 eV. This barrier can be easily overcome by temperature treatment. A similar reaction is calculated for graphene and NiOOH(111). This is shown in Figure S31 in the Supporting Information. One can see that in contrast to Gr@NiOOH(111), there are energy barriers to the detachment of a hydrogen atom from urea. As can be seen from Figure 8, the formation of further products obtained during the reaction has lower energies compared to the initial state.

According to our simulations, the presence of NiOOH(111) combined with graphene leads to a synergetic effect, allowing for a reduction in the activation barrier for hydrogen detachment compared to pure graphene or pure NiOOH(111).

### 3. Conclusion

This work presents a straightforward and promising method for fabricating long nickel nanowires encapsulated in single-walled carbon nanotubes and their application in urea oxidation catalysis. The gold nanowires served as a model system to investigate the formation of nanowires under thermal and plasma treatments. The average length of the nickel nanowires is 410 nm, with some reaching up to 1.2 μm. The formation of such structures can be achieved through a two-step process: first, nitrogen plasma treatment, followed by encapsulation of aqueous nickel chloride and subsequent reduction with hydrazine. Moreover, the nickel nanowires encapsulated in the SWCNTs were tested in UOR. The material maintained stable currents throughout 1000 cycles and 16 h of chronoamperometry test with current retention over 90%. This shows that SWCNTs can serve as an excellent protective shell to operate in a harsh environment as well as to reduce the loading of catalyst material. The material exhibits a distinct electrocatalytic activity — ca. 1150 A g<sup>-1</sup> at 1.7 V vs. RHE in UOR — supported by excellent electrical conductivity and large surface area of carbon nanotubes.

### Supporting Information

Supporting Information is available from the Wiley Online Library or from the author.

### Acknowledgements

A.G.N., A.R.V., and A.E.G. acknowledge the Russian Science Foundation Grant No. 22-13-00436 (P), including its prolongation phase marked by (P), for the support of the synthesis of SWCNTs. Special thanks to Pavel R. Kazansky for TEM measurements.

### Conflict of Interest

The authors declare no conflict of interest.

### Data Availability Statement

The data that support the findings of this study are available from the corresponding author upon reasonable request.

### Keywords

electrochemistry, molecular dynamics, nanostructures, nanotubes, nickel, plasma chemistry

Received: June 17, 2025

Revised: August 28, 2025

Published online:

- [1] T. Matthews, S. P. Mbokazi, T. H. Dolla, S. S. Gwebu, K. Mugadza, K. Raseruthe, L. L. Sikeyi, K. A. Adegoke, O. D. Saliu, A. S. Adekunle, P. Ndungu, N. W. Maxakato, *Small Sci.* **2024**, *4*, 2300057.
- [2] J. Mujtaba, A. Kuzin, G. Chen, F. Zhu, F. S. Fedorov, B. Mohan, G. Huang, V. Tolstoy, V. Kovalyuk, G. N. Goltsman, D. A. Gorin, A. G. Nasibulin, S. Zhao, A. A. Solovev, Y. Mei, *Adv. Mater. Technol.* **2024**, *9*, 2302052.
- [3] Y. M. T. A. Putri, M. I. Syauqi, I. Rahmawati, A. Aliyah, A. R. Sanjaya, T. A. Ivandini, *ChemElectroChem* **2024**, *11*, 2300637.
- [4] X. Zhang, S. Feizpoor, M. Humayun, C. Wang, *Chem. Catalysis* **2024**, *4*, 100840.
- [5] D. Zhu, H. Zhang, J. Miao, F. Hu, L. Wang, Y. Tang, M. Qiao, C. Guo, *J. Mater. Chem. A Mater.* **2022**, *10*, 3296.
- [6] K. Anuratha, M. Rinawati, T.-H. Wu, M.-H. Yeh, J.-Y. Lin, *Nanomaterials* **2022**, *12*, 2970.
- [7] X. Sun, R. Ding, *Catal. Sci. Technol.* **2020**, *10*, 1567.
- [8] Y. Ma, C. Ma, Y. Wang, K. Wang, *2022, Catalysts*, *12*, 337.
- [9] K. Ye, D. Zhang, F. Guo, K. Cheng, G. Wang, D. Cao, *J. Power Sources* **2015**, *283*, 408.
- [10] D. Wang, W. Yan, S. H. Vijapur, G. G. Botte, *J. Power Sources* **2012**, *217*, 498.
- [11] W. Yan, D. Wang, L. A. Diaz, G. G. Botte, *Electrochim. Acta* **2014**, *134*, 266.
- [12] N. A. M. Barakat, M. Motlak, Z. K. Ghouri, A. S. Yasin, M. H. El-Newehy, S. S. Al-Deyab, *J. Mol. Catal. A Chem.* **2016**, *421*, 83.
- [13] A. V. Munde, B. B. Mulik, P. P. Chavan, B. R. Sathe, *Electrochim. Acta* **2020**, *349*, 136386.
- [14] L. N. Quan, J. Kang, C. Z. Ning, P. Yang, *Chem. Rev.* **2019**, *119*, 9153.
- [15] M. Ma, C. M. Fernandes, M. Li, A. C. A. Pinto, C. M. Alves, D. F. Franceschini, E. M. Rodrigues, E. A. Ponzio, J. C. M. Silva, Y. Xing, *J. Clust. Sci.* **2024**, *35*, 79.
- [16] M. A. Ghanem, A. M. Al-Mayouf, J. P. Singh, P. Arunachalam, *Electrocatalysis* **2017**, *8*, 16.
- [17] S. Zhou, L. Shi, Y. Li, T. Yang, S. Zhao, *Adv. Funct. Mater.* **2024**, *34*, 2400767.
- [18] Y. u. Zhang, W. Chi, Z. Yin, X. Ma, Y. Zhou, W. Liu, J. Li, *J. Alloys Compd.* **2024**, *1002*, 175383.
- [19] T. Rajala, R. Kronberg, R. Backhouse, M. E. M. Buan, M. Tripathi, A. Zitolo, H. Jiang, K. Laasonen, T. Susi, F. Jaouen, T. Kallio, *Appl. Catal. B* **2019**, *265*, 118582.
- [20] Z. Chen, R. Wu, Y. Liu, Y. Ha, Y. Guo, D. Sun, M. Liu, F. Fang, *Adv. Mater.* **2018**, *30*, 1802011.
- [21] C. He, N. Zhao, C. Shi, E. Liu, J. Li, *Adv. Mater.* **2015**, *27*, 5422.

- [22] A. Loiseau, N. Demonty, O. Stéphan, C. Colliex, H. Pascard, *Fill-ing Carbon Nanotubes Using an Arc Discharge*, Springer, Boston, MA, 2002.
- [23] D. Haase, S. Hampel, A. Leonhardt, J. Thomas, N. Mattern, B. Büchner, *Surf. Coat. Technol.* **2007**, 201, 9184.
- [24] M. O. Bulavskiy, F. S. Fedorov, A. G. Nasibulin, *Surf. Interfaces* **2024**, 46, 104019.
- [25] M. V. Kharlamova, C. Kramberger, *Nanomaterials* **2023**, 13, 314.
- [26] Y. A. Kim, H. Muramatsu, T. Hayashi, M. Endo, M. Terrones, M. S. Dresselhaus, *Chem. Phys. Lett.* **2004**, 398, 87.
- [27] J. M. Skowroński, P. Scharff, N. Pfänder, S. Cui, *Adv. Mater.* **2003**, 15, 55.
- [28] S. Sahebian, S. M. Zebarjad, J. vahdati Khaki, A. Lazzeri, *J Nanostr. Chem.* **2015**, 5, 287.
- [29] M. V. Kharlamova, *Nanomaterials* **2022**, 13, 176.
- [30] X. Zhao, J. Li, J. Zhang, J.-H. Yang, *Ionics (Kiel)* **2023**, 29, 2969.
- [31] E. Burresi, M. L. Protopapa, *Carbon Trends* **2024**, 17, 100412.
- [32] D. E. Glass, V. Galvan, G. K. S. Prakash, *Electrochim. Acta* **2017**, 253, 489.
- [33] Q. Zhang, F. M. d. Kazim, S. Ma, K. Qu, M. Li, Y. Wang, H. Hu, W. Cai, Z. Yang, *Appl. Catal. B* **2021**, 280, 119436.
- [34] Y. Ma, C. Ma, Y. Wang, K. Wang, *Catalysts* **2022**, 12, 337.
- [35] I. V. Anoshkin, A. G. Nasibulin, Y. Tian, B. Liu, H. Jiang, E. I. Kauppinen, *Carbon N Y* **2014**, 78, 130.
- [36] P. Korusenko, K. Kharisova, E. Knyazev, O. Levin, A. Vinogradov, E. Alekseeva, *Appl. Sci. (Switzerland)* **2023**, 13, 1911057.
- [37] K. K. Zamansky, A. A. Osipova, F. S. Fedorov, D. S. Kopylova, V. Shunaev, A. Alekseeva, O. E. Glukhova, A. G. Nasibulin, *Appl. Surf. Sci.* **2023**, 640, 158334.
- [38] T. N. Kurtukova, D. S. Kopylova, N. I. Raginov, E. M. Khabushev, I. V. Novikov, S. I. Serebrennikova, D. V. Krasnikov, A. G. Nasibulin, *Appl. Phys. Lett.* **2023**, 122, 093501.
- [39] M. Seredych, A. V. Tarnashausky, T. J. Bandosz, *Adv. Funct. Mater.* **2010**, 20, 1670.
- [40] A. Kovtun, D. Jones, S. Dell'Elce, E. Treossi, A. Liscio, V. Palermo, *Carbon N Y* **2019**, 143, 268.
- [41] A. Misra, P. K. Tyagi, M. K. Singh, D. S. Misra, *Diam. Relat. Mater.* **2006**, 15, 385.
- [42] S. Hussain, R. Amade, E. Jover, E. Bertran, *J. Mater. Sci.* **2013**, 48, 7620.
- [43] O. T. Zaremba, A. E. Goldt, E. M. Khabushev, A. S. Anisimov, A. G. Nasibulin, *Mater. Sci. Eng. B* **2022**, 278, 115648.
- [44] X. P. Gao, Y. Zhang, X. Chen, G. L. Pan, J. Yan, F. Wu, H. T. Yuan, D. Y. Song, *Carbon N Y* **2004**, 42, 47.
- [45] D. I. Dimitrov, A. Milchev, K. Binder, *Phys. Rev. Lett.* **2007**, 99, 1.
- [46] M. Wortmann, K. Viertel, M. Westphal, D. Graulich, Y. Yang, M. Gärner, J. Schmalhorst, N. Frese, T. Kuschel, *Small Methods* **2024**, 8, 2300944.
- [47] V. V. Kaichev, D. Teschner, A. A. Saraev, S. S. Kosolobov, A. Y. Gladky, I. P. Prosvirin, N. A. Rudina, A. B. Ayupov, R. Blume, M. Hävecker, A. Knop-Gericke, R. Schlögl, A. V. Latyshev, V. I. Bukhtiarov, *J. Catal.* **2016**, 334, 23.
- [48] A. N. Mansour, C. A. Melendres, *Surf. Sci. Spectra* **1994**, 3, 271.
- [49] K. K. Lian, D. W. Kirk, S. J. Thorpe, *J. Electrochem. Soc.* **1995**, 142, 3704.
- [50] I. V. Novikov, D. V. Krasnikov, E. M. Khabushev, V. S. Shestakova, Y. E. Matyushkin, A. G. Nasibulin, *Carbon* **2024**, 217, 118589.
- [51] B. S. Yeo, A. T. Bell, *J. Phys. Chem. C* **2012**, 116, 8394.
- [52] A. Shekhawat, R. Samanta, S. Panigrahy, S. Barman, *ACS Appl. Energy Mater.* **2023**, 6, 3135.
- [53] N. A. M. Barakat, M. A. Yassin, A. S. Yasin, S. Al-Meer, *Int. J. Hydrogen Energy* **2017**, 42, 21741.
- [54] Z. Zhu, K. Ge, Z. Li, J. Hu, P. Chen, H. Bi, *Small* **2023**, 19, 2205234.
- [55] F. S. Alamro, S. S. Medany, N. S. Al-Kadhi, H. A. Ahmed, M. A. Hefnawy, *Molecules* **2024**, 29, 1215.
- [56] S. A. Aladeemy, P. Arunachalam, M. S. Amer, A. M. Al-Mayouf, *RSC Adv.* **2025**, 15, 14.
- [57] H. M. Youssef, M. N. Shaddad, S. A. Aladeemy, A. M. Aldawsari, *Catalysts* **2025**, 15, 652.
- [58] L. Zhang, Y. Chao, K. Yang, D. Xue, S. Zhou, *Front. Chem.* **2022**, 9, 782307.
- [59] H. K. Jung, H. W. Lee, *J. Nanomater.* **2014**, 2014, 270989.
- [60] L. Trotocaud, S. L. Young, J. K. Ranney, S. W. Boettcher, *J. Am. Chem. Soc.* **2014**, 136, 6744.
- [61] Y. Feng, N. Ran, X. Wang, Q. Liu, J. Wang, L. Liu, K. Suenaga, W. Zhong, R. Ma, J. Liu, *Adv. Energy Mater.* **2023**, 13, 2302452.
- [62] J. Ge, J. Kuang, Y. Xiao, M. Guan, C. Yang, *Surf. Interfaces* **2023**, 41, 103230.